JOURNAL OF THEORETICAL AND APPLIED MECHANICS
60, 3, pp. 347-360, Warsaw 2022
https://doi.org/10.15632/jtam-pl/150588

CFD-PREDICTED ROTORDYNAMIC CHARACTERISTICS OF A HIGH TEMPERATURE SODIUM LIQUID SEAL[1]

Tong Wang
School of Mechanical and Powder Engineering, Harbin University of Science and Technology, Harbin, China

Pingwei Chen
School of Mechanical and Powder Engineering, Harbin University of Science and Technology, Harbin, China, and Chongqing Pump Industry, Chongqing, China
Corresponding author Pingwei Chen, e-mail: 297183138@qq.com

Wensheng Ma
Chongqing Pump Industry, Chongqing, China, and Harbin Engineering University, Harbin, China
e-mail: 48200085@qq.com

Guangbin Yu
Harbin Institute of Technology, Harbin, China

Rotordynamic characteristics of a high temperature sodium liquid (HTSL) seal were studied in this paper by using CFD software. Compared with the water liquid seal, the HTSL seal has a larger leakage flow rate and a lower drag power loss. The HTSL seal has a larger direct stiffness coefficient and the effective stiffness coefficient K_{eff} is also larger than the water liquid seal, which means the HTSL seal has a better stiffness capacity. The HTSL seal possesses a positive effective damping coefficient C_{eff} in the whole whirling frequency range, which means better stability for the rotor system especially in high rotor speeds.

Keywords: sodium liquid seal, multi-frequency whirling model, rotordynamic characteristics, CFD

1. Introduction

In order to solve the situation that the uranium fuel is facing depletion, fast neutron reactors (Fast Reactor) have attracted increasing attention in many countries (Feng, 2003). At present, with the rapid development of the 4-th generation nuclear energy technology, the sodium-cooled fast reactor technology has become the first choice for the fourth generation nuclear energy system as a way to solve the problem of energy supply (Xu and Yang, 2016; Chen *et al.*, 2018). Whether it is used as a primary-circuit sodium pump or a secondary-circuit sodium pump (Dong, 2013), the fluid medium is a high temperature sodium liquid. Different from the traditional liquid medium, like water or oil, the high temperature sodium liquid is a special liquid medium with very low viscosity. The thermal conductivity of the sodium liquid is also much larger than the water liquid, and can quickly and effectively remove the heat which is generated by the core of a nuclear reactor, so the sodium liquid is an efficient coolant.

Like many other particular fluid media, many analysis methods are based on CAE (Computer Aided Engineering) simulation (Chen *et al.*, 2019; Huang *et al.*, 2015), especially for such a high temperature medium. The impeller and bearing are the core components of the sodium pump,

[1]Paper presented at the 5th International Conference on Material Strength and Applied Mechanics, MSAM-2022, Qingdao, Shandong, China

now the research on the sodium pump mainly focuses on the influence of a high temperature sodium solution on the hydraulic performance and influence on the hydro-hybrid bearing (Ko and Kim, 2015; Yang *et al.*, 2015; Xie *et al.*, 2018; Pei *et al.*, 2020). With a high speed, high efficiency and structural design requirements of multi-stage sodium pumps, the impeller inter-stage seal is very important. Like other rotating machinery, such as steam turbines, aero-engines and centrifugal pumps, the inter-stage seal has an influence on both the efficiency and the rotordynamic characteristic of the sodium pump. At present, the research on the rotordynamic characteristic of the seal mainly focuses on the normal temperature medium such as water and oil (Zhai *et al.*, 2018; Zhang *et al.*, 2013; Moreland, 2016; Moreland *et al.*, 2018). In terms of numerical calculation, many scholars first used and expanded the bulk-flow model to analyze rotordynamic coefficients of a liquid annular seal (Iwatsubo and Sheng, 1990; Marquette and Childs, 1996). With the development of computer and CFD methods, the quasi-steady method based on CFD software (Xia *et al.*, 2018; Kim and Ha, 2016) and the transient CFD method based on multiple-frequency whirling models (Li *et al.*, 2020) are now the two advanced CFD methods.

The main objective of this paper is to use the CFD method to evaluate the rotordynamic characteristic of the high temperature sodium liquid (HTSL) seal. The HTSL seal is analyzed by using the transient CFD method which is based on the multiple-frequency rotor whirling model. In this paper, the rotordynamic characteristics of the normal temperature water liquid seal were also calculated for comparison. It reveals the frequency-independent rotordynamic coefficients (K, k, C, c, M, m) and the frequency-dependent rotordynamic coefficients (K_{eff}, C_{eff}) under different operation conditions (three pressure drops and three rotor speeds). This study will pave a way for further study on rotordynamic characteristics of the high temperature sodium liquid seal.

2. Computational theory

When a rotor is whirling with small motion which is around its equilibrium position, the force which is induced by the fluid can be written by the following equation

$$-\begin{bmatrix} F_x \\ F_y \end{bmatrix} = \begin{bmatrix} K & k \\ k & K \end{bmatrix} \begin{bmatrix} X \\ Y \end{bmatrix} + \begin{bmatrix} C & c \\ c & C \end{bmatrix} \begin{bmatrix} \dot{X} \\ \dot{Y} \end{bmatrix} + \begin{bmatrix} M & m \\ m & M \end{bmatrix} \begin{bmatrix} \ddot{X} \\ \ddot{Y} \end{bmatrix} \tag{2.1}$$

where $K = K_{xx} = K_{yy}$, $k = K_{xy} = -Kyx$, $C = C_{xx} = C_{yy}$, $c = C_{xy} = -C_{xy}$, $M = M_{xx} = M_{yy}$, $m = M_{xy} = -M_{yx}$.

F_x and F_y are fluid-induced forces in x and y directions [N], K and k are direct stiffness and cross-coupling stiffness coefficients [N/m], C and c are direct damping and cross-coupling damping coefficients [Ns/m], M and m are direct virtual mass and cross-coupling virtual masses [kg]. X and Y are relative small displacements. K_{ij}, C_{ij} and M_{ij} are dynamic coefficients of different directions. Equation (2.1) can be stated in the frequency domain

$$-\begin{bmatrix} F_x(\Omega) \\ F_y(\Omega) \end{bmatrix} = \begin{bmatrix} H_{xx}(\Omega) & H_{yx}(\Omega) \\ H_{xy}(\Omega) & H_{yy}(\Omega) \end{bmatrix} \begin{bmatrix} D_x(\Omega) \\ D_y(\Omega) \end{bmatrix} \tag{2.2}$$

where Ω is the whirling speed, $D_i(\Omega)$ is rotor motion in the i-th direction, $H_{ij}(\Omega)$ are complex force impedances that can be expressed as follows

$$H_{xx} = H_{yy} = \frac{(-F_x)D_x - (F_y)D_y}{D_xD_x + D_yD_y} \qquad H_{xy} = -H_{yx} = \frac{(-F_x)D_y - (-F_y)D_x}{D_yD_y + D_xD_x} \tag{2.3}$$

The relationship between the force impedances and dynamic coefficients can be stated

$$H_{ij} = K_{ij} - \Omega^2 M_{ij} + j(\Omega C_{ij}) \tag{2.4}$$

The real and imaginary part of the force impedance coefficient can be expressed as follows

$$\mathrm{Re}\,(H_{ij}) = K_{ij} - \Omega^2 M_{ij} \qquad \mathrm{Im}\,(H_{ij}) = \Omega C_{ij} \tag{2.5}$$

From formula (2.5), the frequency-independent dynamic coefficients can be obtained by fitting the real and imaginary parts at multiple frequencies.

We assume that the rotor is whirling around its centered position, the tangential and radial forces can be written as

$$\begin{aligned} -\frac{F_t}{e} &= -K_{xy} + \Omega^2 M_{xy} + \Omega C_{xx} = -\,\mathrm{Re}\,(H_{xy}) + \mathrm{Im}\,(H_{xx}) \\ -\frac{F_r}{e} &= K_{xx} - \Omega^2 M_{xx} + \Omega C_{xy} = \mathrm{Re}\,(H_{xx}) + \mathrm{Im}\,(H_{xy}) \end{aligned} \tag{2.6}$$

The effective stiffness and the effective damping often need the overall stability characteristics to be analyzed. They are expressed as

$$\begin{aligned} K_{\mathit{eff}} &= -\frac{F_r}{e} = \mathrm{Re}\,(H_{xx}) + \mathrm{Im}\,(H_{xy}) \\ C_{\mathit{eff}} &= \Big(-\frac{F_t}{e}\Big)\frac{1}{\Omega} = [-\,\mathrm{Re}\,(H_{xy}) + \mathrm{Im}\,(H_{xx})]\frac{1}{\Omega} \end{aligned} \tag{2.7}$$

From this formula, we notice that the frequency-dependent effective stiffness K_{eff} is a combination of K, M, c, the frequency-dependent effective damping C_{eff} is a combination of k, m, C.

The whirling displacement and whirling velocity of the rotor are periodic signals in the time domain. Assuming that the rotor is excited by multiple whirling frequencies, the fluid induced forces are also multi-frequency periodic signals in the time domain. In order to analyze the effect of different whirling frequencies on the rotordynamic characteristics of the seal, two sets of multi-frequency elliptical orbit equations are introduced as follows

$$x = a\sum_{i=1}^{N}\cos(\Omega_t t) \qquad y = b\sum_{i=1}^{N}\sin(\Omega_t t) \tag{2.8}$$

and

$$x = b\sum_{i=1}^{N}\cos(\Omega_t t) \qquad y = a\sum_{i=1}^{N}\sin(\Omega_t t) \tag{2.9}$$

The elliptical whirling frequencies studied in this paper are 10 Hz, 20 Hz, 30 Hz,..., 120 Hz. The set includes 12 frequencies. In order to satisfy the theory of small displacement disturbance, we assume that $a = 0.01c_r$, $b = 0.005c_r$, where a, b are motion amplitudes and c_r is the seal radial clearance.

Figure 1 gives an example of the whirling model (X direction). The rotor motion is monitored. Figure 2 shows the example of the rotor motion in the time- and frequency-domain. Similarly, the response force in the time- and frequency-domain can also be obtained.

According to Eqs. (2.5), the least squares method is used to $\mathrm{Re}\,(H_{ij})$ versus Ω^2 and $\mathrm{Im}\,(H_{ij})$ versus Ω, respectively. The curve fit plots show a frequency range up to 120 Hz. The slope of the curve $\mathrm{Re}\,(H_{ij})$ gives the direct and cross coupling virtual mass, and its intercept is the direct stiffness and cross coupling stiffness coefficients. The slope of the curve $\mathrm{Im}\,(H_{ij})$ gives the direct and cross coupling damping coefficients. For an incompressible fluid, $\mathrm{Re}\,(H_{ij})$ and $\mathrm{Im}\,(H_{ij})$ are frequency-dependent. The rotordynamic coefficients are frequency-independent. Figure 3 gives an example of linear fit of $\mathrm{Re}\,(H_{xx})$ and $\mathrm{Im}\,(H_{xy})$.

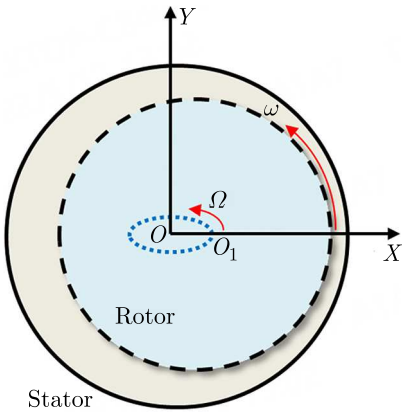

Fig. 1. Whirling model (X excitation)

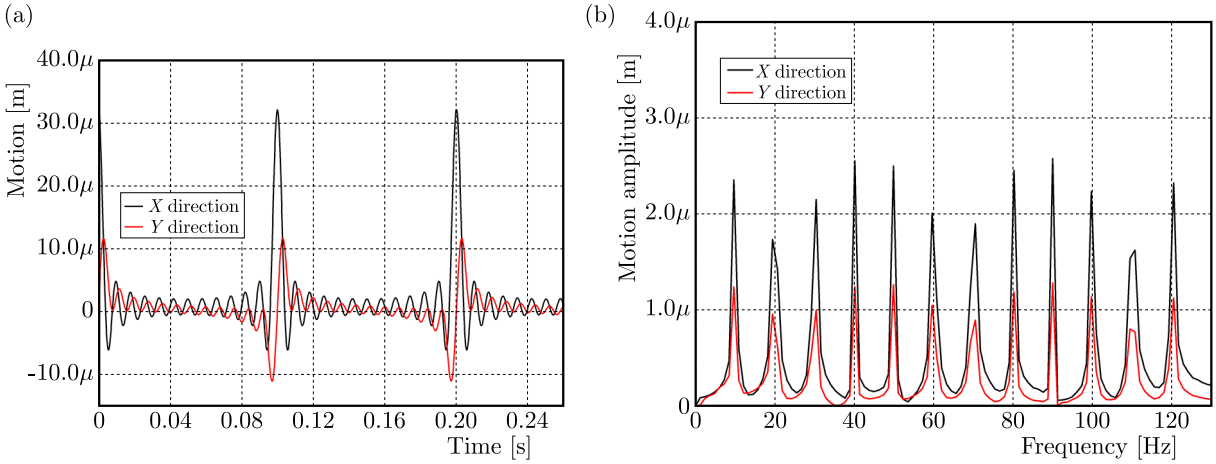

Fig. 2. Rotor motion (x excitation): (a) motion in the time-domain, (b) motion in the frequency-domain

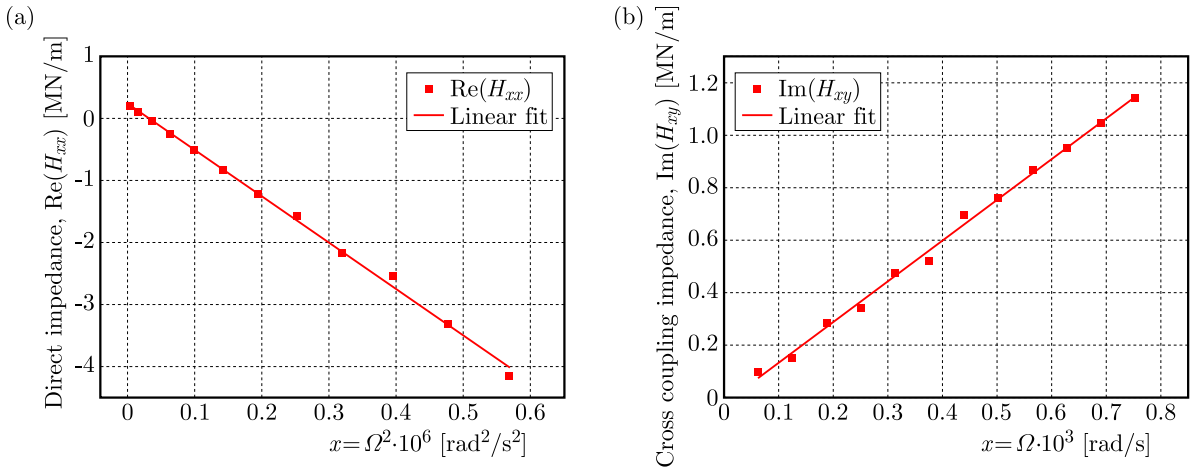

Fig. 3. Linear fit of $\mathrm{Re}\,(H_{xx})$ and $\mathrm{Im}\,(H_{xy})$: (a) direct impedance $\mathrm{Re}\,(H_{xx})$, (b) cross coulping impendance $\mathrm{Im}\,(H_{xy})$

3. Calculation model

In this paper, we choose the same geometry of the seal for comparison of the water liquid and the high temperature sodium liquid. Table 1 shows the physical property parameters of the high temperature sodium liquid and the water liquid. Figure 4 illustrates geometry of the grooved seal with parallel grooves on the rotor.

Table 1. Physical property

	Sodium liquid	Water
T [°C]	350	20
ρ [kg/m^3]	868.1	996.9
C [J/kg/K]	1300	4180
μ [Pa s]	3.11e-4	1.0e-3
K [W/m/K]	142	0.598

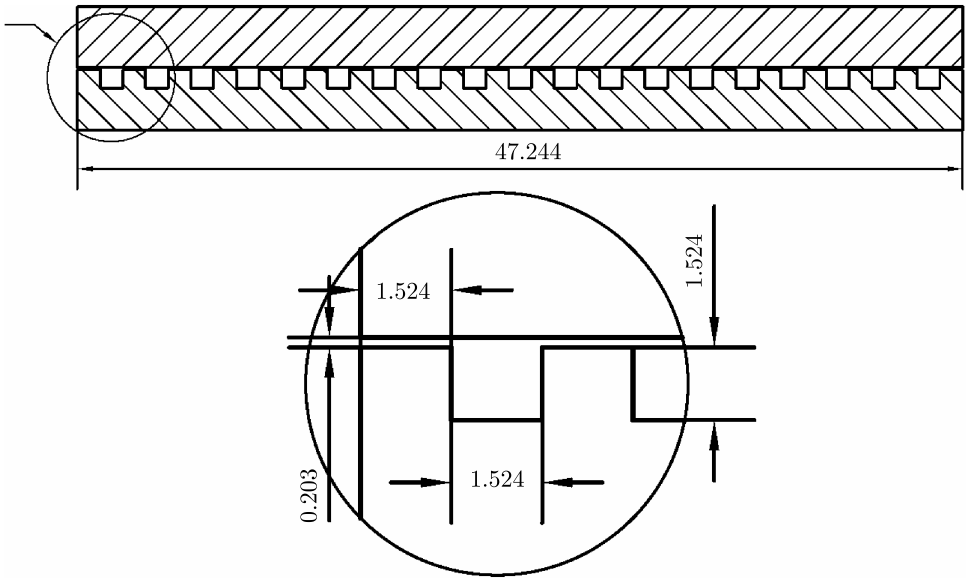

Fig. 4. Geometry of parallel grooved seal

Table 2. Geometry parameters and operational conditions

Inlet pressure [bar]	3.08, 5.12, 9.25
Outlet pressure [bar]	1.0
Inlet preswirl ratio	0
Rotor speed [rpm]	2000, 4000, 6000
Rotor diameter [mm]	102
Seal radial clearance [mm]	0.203
Groove depth [mm]	1.524
Land width [mm]	1.524
Groove length [mm]	1.524

The geometry parameters and operational conditions can be seen in Table 2. This analysis has been done at three different pressure drops and three rotor speeds. Figure 5 illustrates the 3D model and mesh in Fluent software. The meshes are all hexahedron elements, and the mesh-

-independence study is verified, which can be seen Fig. 6. The final mesh size of the CFD model used in this paper is 2736000 elements (3000300 nodes).

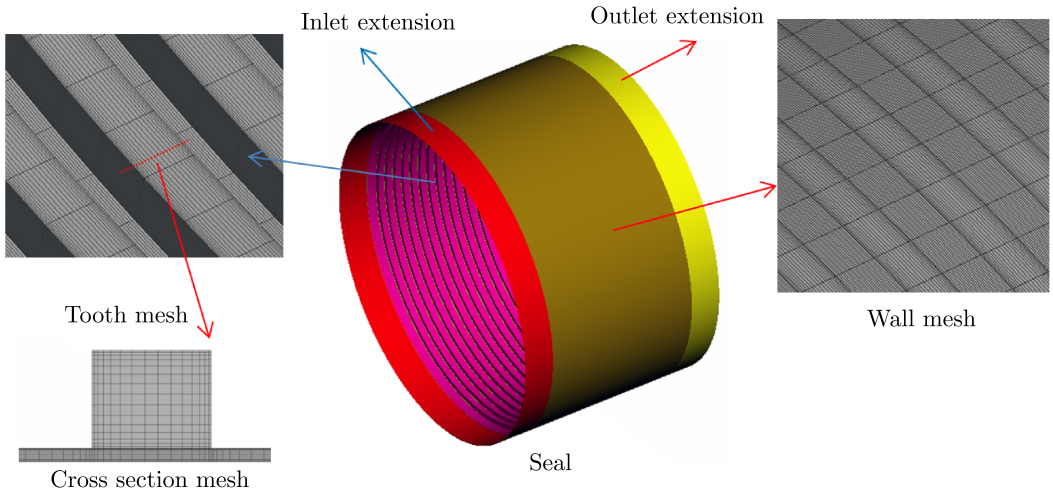

Fig. 5. Computational model and mesh

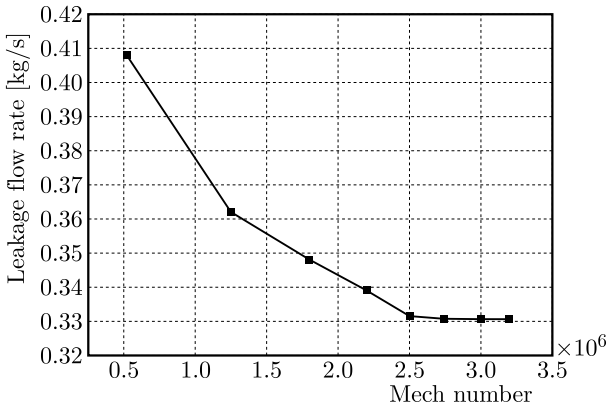

Fig. 6. Mesh independence study

Due to the low viscosity characteristics of the water and high temperature sodium liquids, the k-ε turbulence models are more suitable in CFD software. Table 3 gives the transient CFD solution setups. The inlet and outlet boundaries are the pressure inlet and outlet boundary conditions. The wall properties are adiabatic and non-slip boundary conditions. In the transient CFD solution, the sampling frequency is 10000 Hz and the time step is 0.0001 s. We choose the total sampling time 0.5 s.

Table 3. CFD method

Fluids	Sodium liquid(350°C)/water(20°C)
Inlet boundary condition	Total pressure
Outlet boundary condition	Static pressure
Solution type	Transient
Mesh motion	Dynamic mesh method
Turbulence model	Scalable wall function, k-ε model
Wall property	Adiabatic

4. Calculation model results and discussion

4.1. Experimental results

To prove the authenticity of CDF calculation, a seal test rig with normal temperature water is used for the experiments, which is shown in Fig. 7.

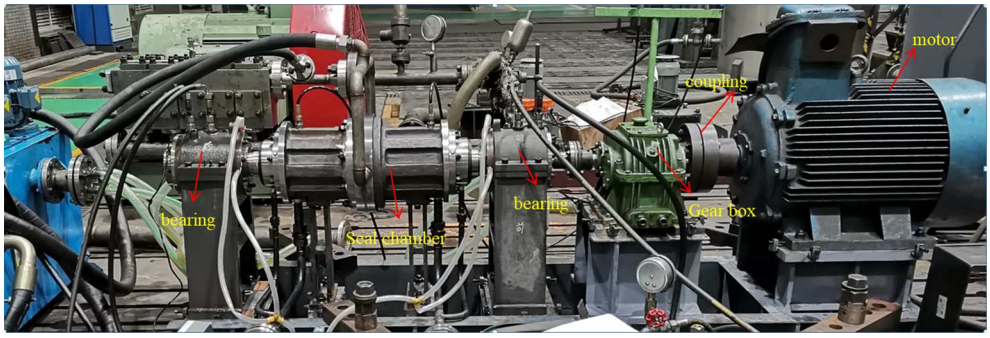

Fig. 7. Test rig

Figure 8a and 8b give a comparison between the test and calculation results of the leakage flow rate and drag power loss. The drag power loss can be defined as

$$W = \frac{Tn}{9550} \tag{4.1}$$

where T is the friction torque [Nm], n is the rotor speed [r/min].

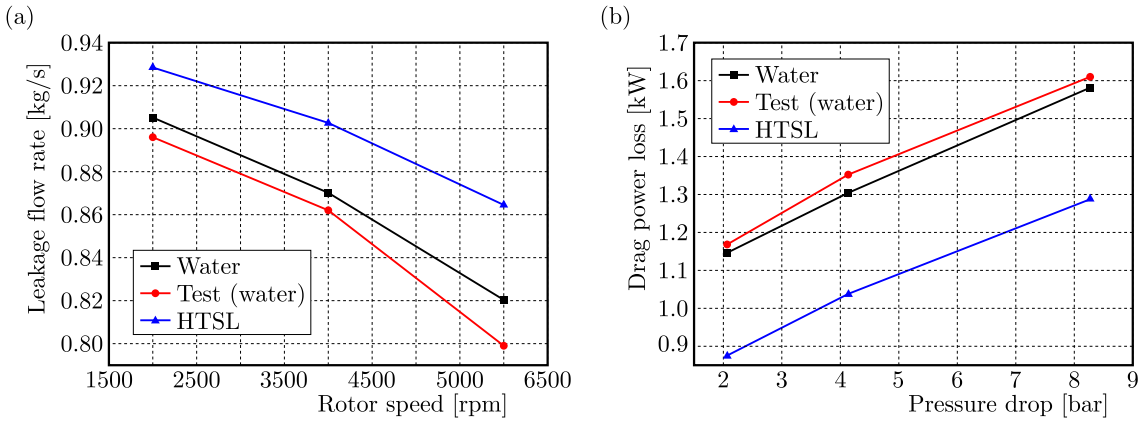

Fig. 8. Calculations versus measured parameters: (a) leakage flow rate ($\Delta p = 8.27$ bar), (b) drag power loss ($n = 2000$ rpm, $\lambda = 0$)

It can be seen that the test results of the leakage and drag power loss are basically the same as the calculation results, and the relative deviations are small, the maximum deviation is about 3.5%.

The leakage flow rate for both two seals decreases with an increase of the rotor speed. This is because the rotation effect caused by the rotor makes the leakage fluid in the cavity rotate along the circumferential direction. As the rotor speed increases, the rotation effect increases too, so the leakage flow rate decreases.

The drag power loss for the HTSL seal is lower than the water liquid seal. This is due to the lower viscous force caused by the rotor.

The results show that the CFD model is correct and can be used for dynamic calculation of high temperature sodium liquids.

4.2. Effects of pressure drop

The CFD method has been used to analyze the influence of pressure drops on the rotordynamic coefficients. It was carried out at three different pressure drops of 2.08 bar, 4.12 bar and 8.25 bar for the two seals.

Figure 9 shows the curve plots of rotordynamic coefficients and pressure drop for two liquids seals ($n = 2000$ min), the rotordynamic coefficients is frequency-independent. For two liquids seals, the direct stiffness K shows an obvious increase with growth of pressure drops. This phenomenon can be explained by the fact that with an increase of the pressure drop, the Lomakin effect will increase too.

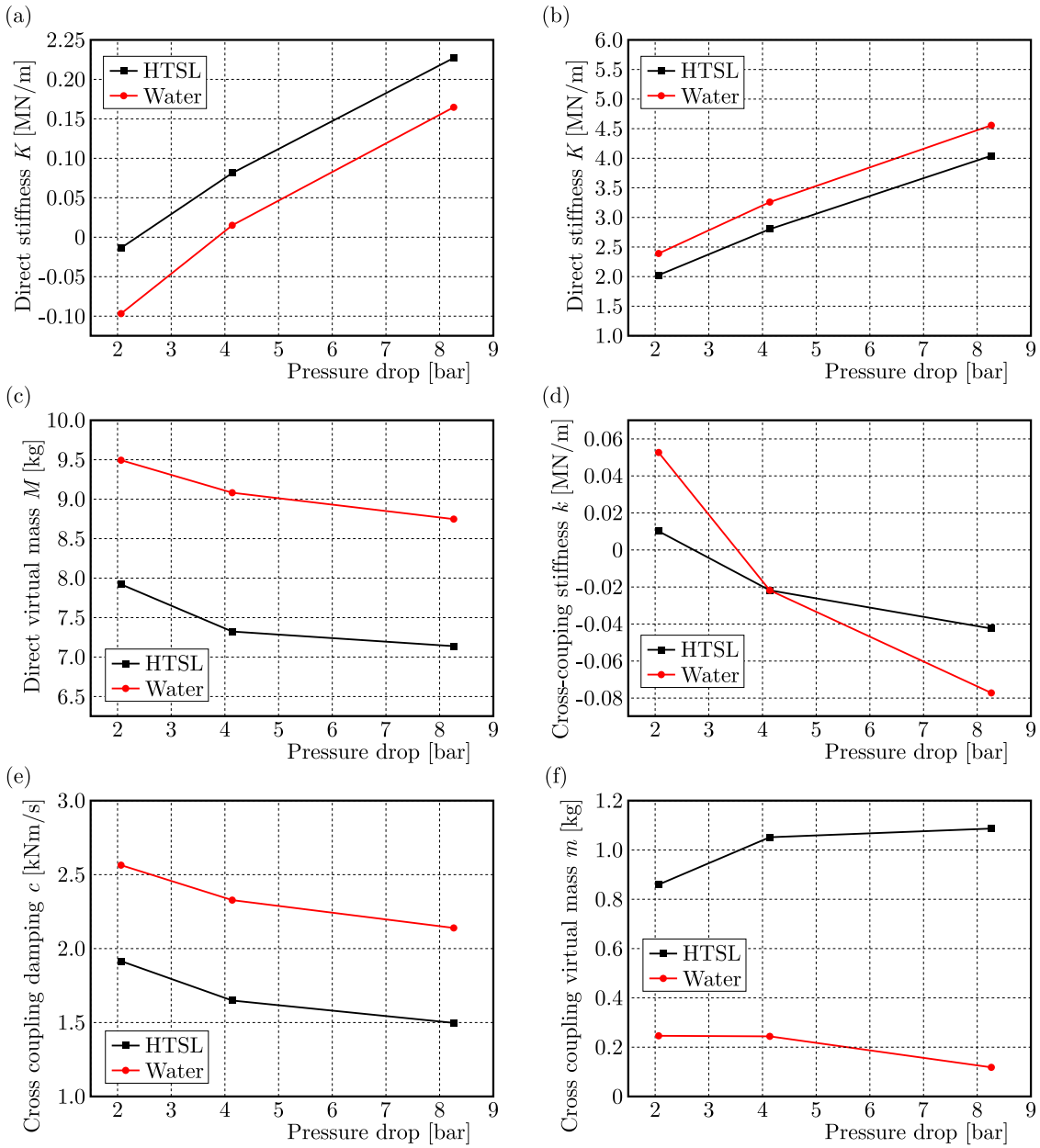

Fig. 9. Rotordynamic coefficients and pressure drop ($n = 2000$ rpm)

The K for HTSL seal is larger ($38 \sim 454\%$) than that for the water liquid seal. The direct virtual mass M is positive and shows a decrease for two steals (10% for HTSL seal, 8% for water liquid seal from 2.08 bar to 8.25 bar). The M of the water liquid seal is larger ($19 \sim 24\%$) than

of the HTSL seal. The cross-coupling damping c for two seals is also positive and illustrates a decrease with the increasing pressure drops (22% for HTSL seal, 17% for water liquid seal from 2.08 bar to 8.25 bar). The c of the water liquid seal is larger ($33 \sim 43\%$) than of the HTSL seal.

The frequency-dependent effective stiffness coefficient K_{eff} is related to K, M and c. It can be seen from Fig. 8a that two seals have small positive K_{eff} at a lower frequency range and display a parabolic decay trend. With an increasing pressure drop, the K_{eff} of the two seals exhibits a slight increase. It can also be seen that K_{eff} for the HTSL seal is larger ($5 \sim 40\%$) than that for water liquid seal. It is the K, M and c that gives a combined effect.

The direct damping C for two seals shows an increase with growth of pressure drops (99% for HTSL seal, 90% for water liquid seal from 2.08 bar to 8.25 bar). The C for the water liquid seal is larger ($12 \sim 18\%$) than for the HTSL seal. There is a decrease in the cross coupling stiffness k with an increase of pressure drops (-0.05 MN/m for HTSL seal, -0.13 MN/m for the water liquid seal from 2.08 bar to 8.25 bar).

Figure 8b shows the plot of the frequency-dependent effective damping coefficient C_{eff} which is affected by C, k and m. Two seals possess a positive C_{eff} in the whole whirling frequency range. The C_{eff} for seals exhibits an obvious increase with an increase of pressure drop. There is little difference between the two values (> 20 Hz), the maximum difference is 10%.

From Figs. 10a,b and formula (2.7), we know that the K_{eff} is equivalent to the radial force, C_{eff} is the ratio of the tangential force to whirling frequency. With an increase of pressure drop, both K_{eff} and C_{eff} increase. The reason is that when the pressure drop increases, the fluid bearing effect grows, and the fluid-induced forces also increase. The radial force for the HTSL seal is slightly larger than for the water liquid seal.

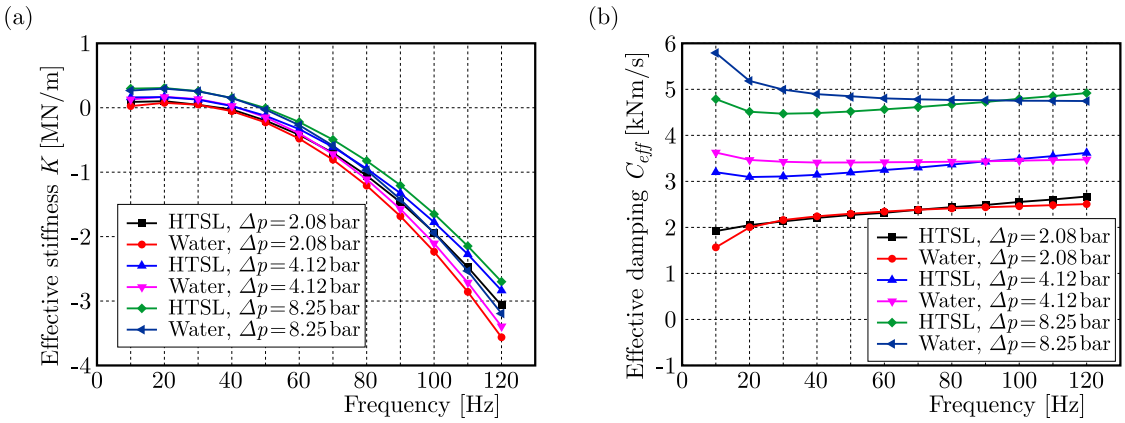

Fig. 10. The effective stiffness (a) and damping (b) at different pressure drops ($n = 2000$ rpm)

4.3. Influence of rotor speed

To investigate the influence of the rotor speed on the rotordynamic characteristics, CFD solutions have been found at rotor speeds of 2000 rpm, 4000 rpm and 6000 rpm for the two seals. Figure 11 shows the change in values of rotordynamic coefficients and rotor speed ($\Delta p = 8.25$ bar).

With an increase of the rotor speed, the direct stiffness K illustrates a decrease trend. It also means an increase in the absolute value of its negative K. This is because that with an increase of the rotor speed, the fluid bearing effect increases. The fluid-induced radial force, which is consistent with the eccentric direction of the rotor, will increase (Childs, 2013).

The K for the HTSL seal is larger ($33 \sim 100\%$) than that for water liquid seal. The direct virtual mass M is positive for two seals and shows an increase from $n = 2000$ rpm to $n = 4000$ rpm, but a decrease from $n = 4000$ rpm to $n = 6000$ rpm. The M of the water liquid

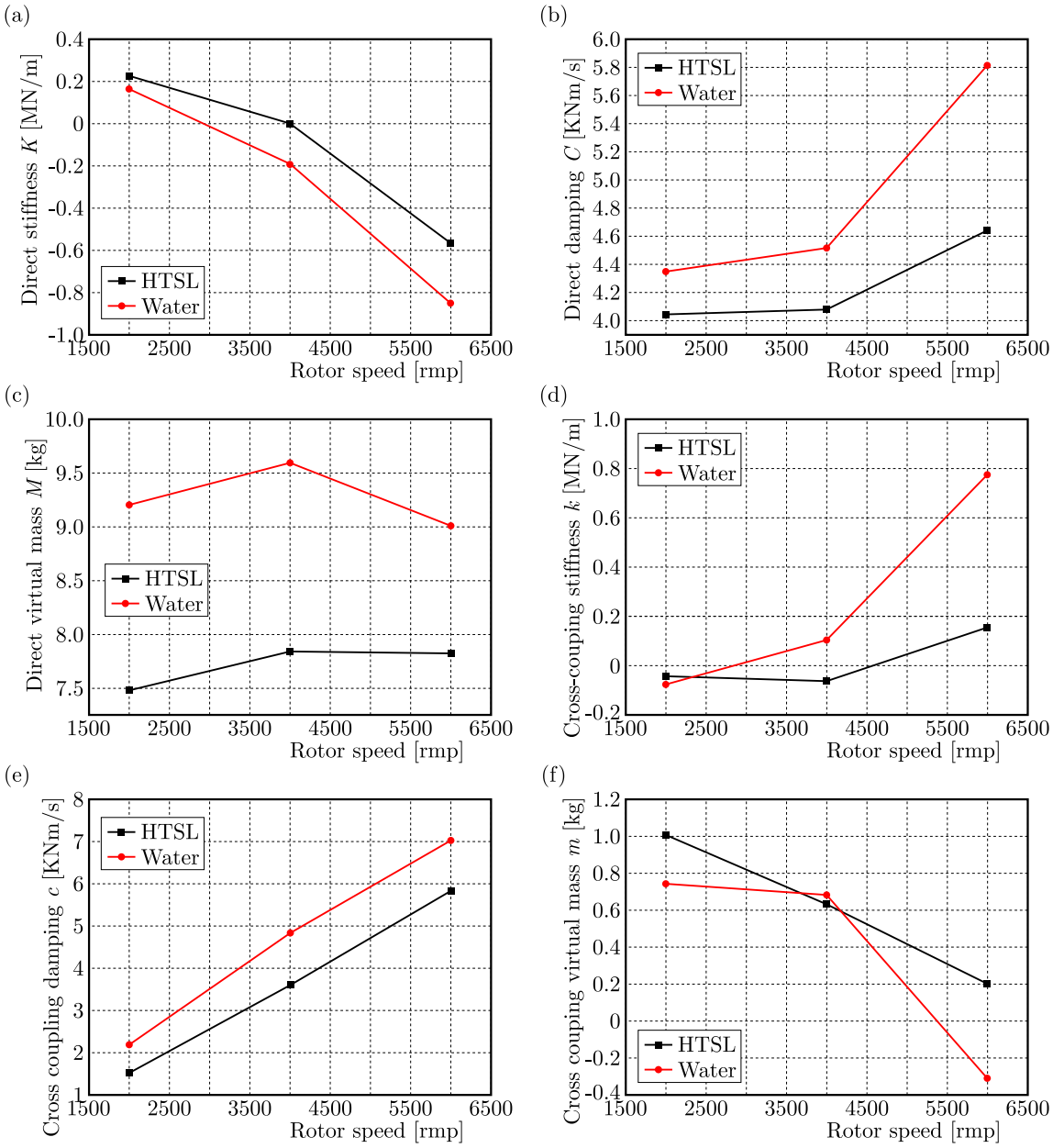

Fig. 11. Rotordynamic coefficients and rotor speed ($\Delta p = 8.25$ bar)

seal is larger ($15 \sim 23\%$) than that of the HTSL seal. The cross-coupling damping c for the two seals shows an increase with the increase of rotor speed (248% for HTSL seal, 221% for the water liquid seal from 2000 rpm to 6000 rpm). The c of the water liquid seal is larger ($20 \sim 44\%$) than that of the HTSL seal.

The plot of the frequency-dependent effective stiffness coefficient K_{eff} can be seen in Fig. 12a. Two seals show a parabolic trend, and the effect of the rotor speed is mainly in the high frequency range (> 50 Hz). In the high frequency range, the negative value of K_{eff} increases with an increase of the rotor speed. It can also be seen that there is a weak difference between K_{eff} of the two seals.

The direct damping C for the two seals shows an increase with the increase of the rotor speed (14% for the HTSL seal, 33% for the water liquid seal from 2000 rpm to 6000 rpm). The C for the water liquid seal is larger than for the HTSL seal. The cross-coupling stiffness k shows an increase with the increase of the rotor speed (0.19 MN/m for HTSL seal, 0.85 MN/m for the

water liquid seal from 2000 rpm to 6000 rpm). Generally speaking, with an increase of the rotor speed, the circumferential flow in the seal cavity and clearance increase, which will cause an increase in the cross-coupled stiffness. Since water has a higher viscosity, the circumferential flow velocity is larger. The cross-coupling virtual mass m shows a decrease with the increase of rotor speed.

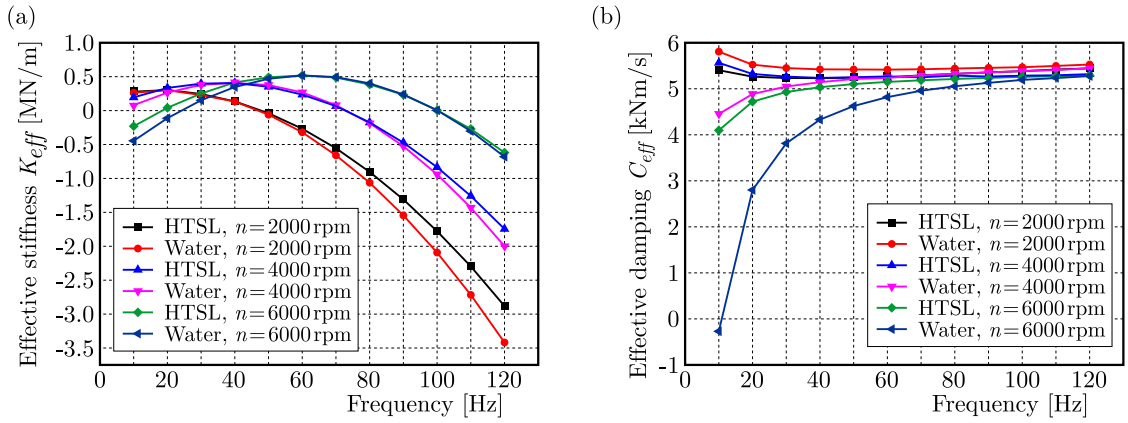

Fig. 12. The effective stiffness (a) and damping (b) at different rotor speeds ($\Delta p = 8.25$ bar)

Figure 12b shows the plot of the frequency-dependent effective damping coefficient C_{eff}. For three rotor speeds, the HTSL seal has a positive C_{eff} in the whole frequency range and the effect of the rotor speed is relatively weak. The C_{eff} for the water liquid seal has an obvious negative value at a very low frequency ($n = 6000$ rpm). For high rotor speeds, the HTSL seal has a larger C_{eff}, this means it is more stable for the rotor system.

4.4. Velocity distribution

In order to know velocity distributions along the cavity height and along the axial direction, we choose 3 cavities, the first cavity (cavity 1), the middle cavity (cavity 8), and the last cavity (cavity 15). The abscissa is the height of the cavity, the larger the abscissa value, the closer to the stator wall.

It can be seen from Fig. 13 ($n = 6000$ rpm, $\Delta p = 2.08$ bar) that the largest velocity is the circumferential velocity in the cavity, followed by the axial velocity, and the radial velocity has the lowest value. When the cavity height is small, the axial flow velocity in the three cavities is negative, indicating that there is a vortex in the cavity. The negative value of the axial velocity is large when it is close to the rotor wall. The axial velocity also increases with an increase of the cavity height. In 15-th cavity, the axial velocity of the sodium liquid reaches 5.42 m/s, while the axial velocity of the water liquid is 4.06 m/s, which indicates that the leakage flow rate of the sodium liquid seal is larger than that of the water liquid seal. Figure 13b shows the radial velocity of the two liquids seals. It can be seen from the figure that the radial flow velocity in the cavity and the gap of the sodium liquid seal is greater than that of the water seal. This means that the fluid bearing effect of the sodium liquid seal is bigger than the water liquid seal, indicating a larger direct stiffness K. Figure 13c illustrates the values of the circumferential velocity of the two liquids seals. When the cavity height is close to the rotor wall, its circumferential velocity is large. This is largely caused by viscous forces. The circumferential velocity of water is greater than that of the sodium liquid, especially in the first cavity, mainly because of the high viscosity of water caused by rotor rotation. In cavity 8 and cavity 15, there is little difference in the circumferential velocity. This means that the difference of the circumferential velocity in the cavity and the clearance is mainly happened at the entrance section of the seal and has almost the similar velocities at the downstream section. This is because the viscous shear stress

which is caused by rotor spinning has the largest value at the entrance section of the seal. The circumferential velocity of water at cavity 1 is larger than the sodium liquid, which can explain that the cross-coupling stiffness k for the water liquid is larger than that for the HTSL.

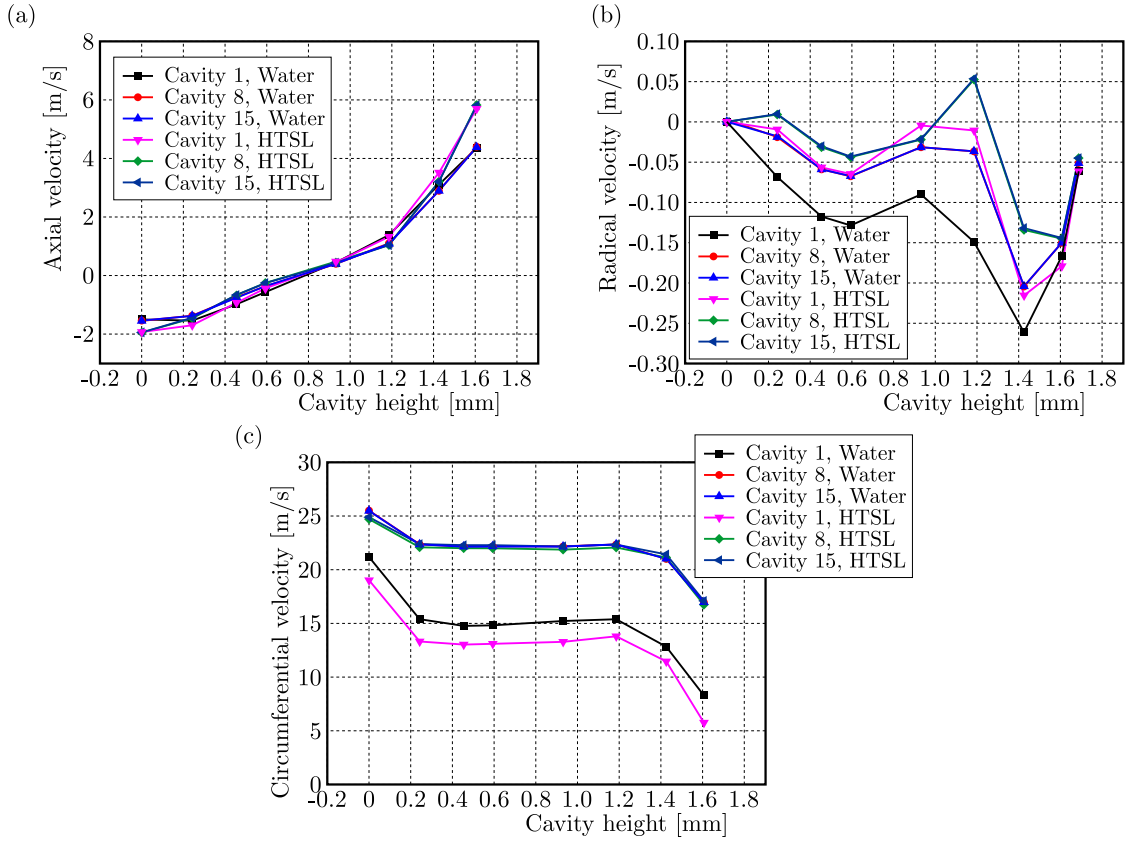

Fig. 13. (a) Axial velocity, (b) radial velocity and (c) circumferential velocity ($n = 6000$ rpm, $\Delta p = 2.08$ bar)

Figure 14 gives a picture of the velocity field on the meridian plane of the last two cavities. When the fluid flows into the cavities, the vortex is formed and the kinetic energy is dissipated, so the pressure reduces and the leakage flow is limited. We can see from the figure that the flow field density in the clearance of the sodium liquid seal is obviously larger than that of the water liquid seal, so the leakage flow rate is larger than that of the water liquid seal.

5. Conclusion

In this paper, we use a multi-frequency whirling model which is based on the CFD method to analyze dynamic characteristics of the high temperature sodium liquid seal (HTSL). The frequency-independent dynamic coefficients, frequency-dependent effective stiffness and the effective damping coefficient are given. The results are compared with the normal temperature water. The effects of different pressure drops and different rotor speeds are considered in the model. From this study, we obtain some conclusions:

- Under the same operational conditions, the leakage flow rate of the high temperature sodium liquid seal is larger than that of the water liquid seal, but the drag power loss is lower. The leakage flow rate shows a decrease with the increasing rotor speed, and the drag power loss shows an increase with the increase of the pressure drop.

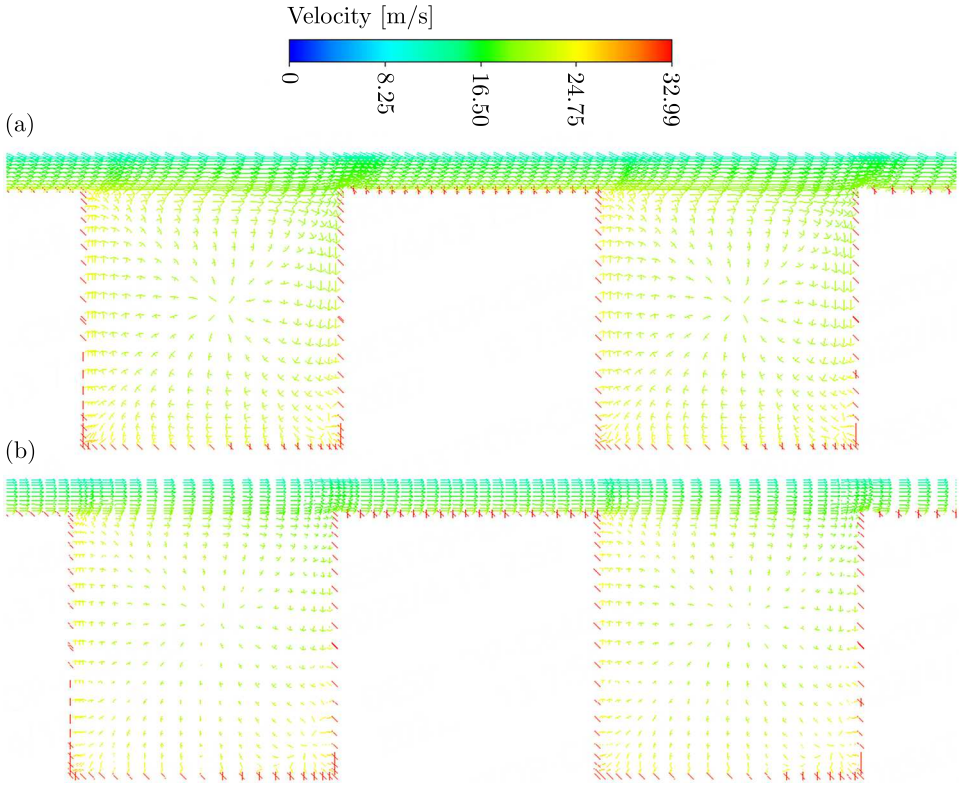

Fig. 14. Flow field on the meridian plane of the last two downstream cavities: (a) HTSL seal, (b) water liquid seal ($n = 6000\,\text{rpm}$, $\Delta p = 2.08\,\text{bar}$)

- For all operational conditions, the high temperature sodium liquid seal has a larger direct stiffness coefficient K than the water liquid seal. The effective stiffness coefficient K_{eff} for the sodium liquid seal is also larger in the whole whirling frequency range. The high temperature sodium liquid seal has a better stiffness capacity.
- For all operational conditions, the high temperature sodium liquid seal possesses positive effective damping coefficients C_{eff} in the whole whirling frequency range. From a rotordynamic point of view, the HTSL seal shows a relatively more stable liquid medium for the rotor system, especially when the rotor speed is high.

Acknowledgments

This work was supported by national key projects, China (No. 2020YFC1512403) and key projects of technological innovation and application development of Chongqing, China (grant No. cstc2020jscx-msxm0411).

References

1. Chen J., Zhang D.L., Song P., Wang X., Wang S., Liang Y., Qiu S.Z., Zhang Y., Wang M., Su G., 2018, CFD investigation on thermal-hydraulic behaviors of a wire-wrapped fuel subassembly for sodium-cooled fast reactor, *Annals of Nuclear Energy*, **113**, 256-269

2. Chen Y., Zhu R., Lu Y., Gao Z., Kang J., 2019, Study on flow field and rotor safety characteristics of MSPs based on flow thermo-coupling, *Processes*, **7**, 10, 711

3. Childs D., 2013, *Turbomachinery Rotordynamics with Case Studies*, Minter Spring Publishing, Wellborn, TX

4. Dong B.B., 2013, Analysis on vibration characteristics of the primary sodium pump of China experimental fast reactor, *Nuclear Science and Engineering*, **33**, 3, 231-237

5. Feng J.T., 2003, *Study of the China Experimental Sodium Pump Fault Diagnosis System* (in Chinese), China Institute of Atomic Energy

6. Huang S., Su X.H., Qiu G.Q., 2015, Transient numerical simulation for solid-liquid flow in a centrifugal pump by DEM-CFD coupling, *Engineering Applications of Computational Fluid Mechanics*, **9**, 1, 411-418

7. Iwatsubo T., Sheng B., 1990, Evaluation of dynamic characteristics parallel grooved annular seals by theory and experiment, *Procedings of IFToMM Third International Conference on Rotordynamics*, Lyon, France, 313-318

8. Kim S.H., Ha T.W., 2016, Prediction of leakage and rotordynamic coefficients for the circumferential-groove-pump seal using CFD Analysis, *Journal of Mechanical Science and Technology*, **30**, 5, 2037-2043

9. Ko S., Kim Y.T., 2015, Numerical study on the main coolant pump of sodium-cooled fast reactor, *Proceedings of ASME/JSME/KSME 2015 Joint Fluids Engineering Conference*, Seoul, South Korea, **1A**, 2

10. Li Z.G., Fang Z., Li J., 2020, A comparison of static and rotordynamic characteristics for two types of liquid annular seals with parallelly grooved stator/rotor, *Journal of Engineering for Gas Turbines and Power*, **142**, 9, 091012

11. Marquette O., Childs D., 1996, An extended three-control-volume theory for circumferentially--grooved liquid seals, *ASME Journal of Tribology*, **118**, 2, 276-285

12. Moreland J.A., 2016, Influence of pre-swirl and eccentricity in smooth stator/grooved rotor liquid annular seals, static and rotordynamic characteristics, M.S. Thesis, Texas A&M University, College Station, TX

13. Moreland J.A., Childs D., Bullock J., 2018, Measured static and rotordynamic characteristics of a smooth-stator/grooved-rotor liquid annular seal, *ASME Journal of Fluid Engineering*, **140**, 10, 101109

14. Pei S., Niu H.J., Hong J., 2020, Lubrication characteristics of hybrid bearing in sodium-cooled fast reactor (in Chinese), *Journal of Mechanical Engineering*, **56**, 29-37

15. Xia P., Liu Z.S., Yu X., Zhao J., 2018, A transient bulk flow model with circular whirl motion for rotordynamic coefficients of annular seals, *Chinese Journal of Aeronautics*, **31**, 5, 1085-1094

16. Xie Z.L., Rao Z.S., Ta N., 2018, Investigation on the lubrication regimes and dynamic characteristics of hydro-hybrid bearing of two-circuit main loop liquid sodium pump system, *Annals of Nuclear Energy*, **115**, 220-232

17. Xu M., Yang H.Y., 2016, Safety properties of sodium-cooled fast reactors (in Chinese), *Physics*, **45**, 9, 561-568

18. Yang H.Y., Liu Y.Z., Yang Y., et al., 2015, Technical progress of 600 MW demonstration fast reactor (CFR600) (in Chinese), *Annual Report of China Academy of Atomic Energy*, **1**, 42-46

19. Zhai L.L., Zhu Z.C., Zhang Z.J., Guo J., Cui B.L., 2018, Theoretical solutions for dynamic characteristics of spiral-grooved liquid seals, *Tribology Transactions*, **62**, 1, 22-33

20. Zhang M., Wang X.F., Xu S.L., Wang W., 2013, Numerical simulation of the flow field in circumferential grooved liquid seals, *Advances in Mechanical Engineering*, **5**

Manuscript received March 18, 2022; accepted for print May 8, 2022